In Situ X-ray Diffraction Studies of (De)lithiation Mechanism in Silicon Nanowire Anodes

Sumohan Misra,[†,#] Nian Liu,[‡,#] Johanna Nelson,[†,∥] Seung Sae Hong,[§] Yi Cui,[⊥,∥,*] and Michael F. Toney[†,∥,*]

[†]Stanford Synchrotron Radiation Lightsource, SLAC National Accelerator Laboratory, 2575 Sand Hill Road, Menlo Park, California 94025, United States, [‡]Department of Chemistry, Stanford University, Stanford, California 94305, United States, [§]Department of Applied Physics, Stanford University, Stanford, California 94305, United States, [⊥]Department of Materials Science and Engineering, Stanford University, Stanford, California 94305, United States, and [∥]Stanford Institute for Materials and Energy Sciences, SLAC National Accelerator Laboratory, 2575 Sand Hill Road, Menlo Park, California 94025, United States. [#]These authors contributed equally to this work.

ABSTRACT

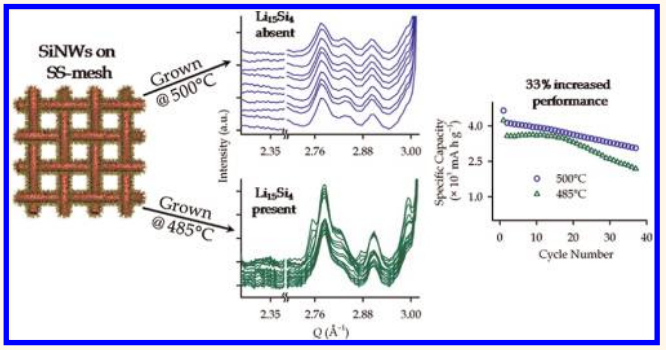

Silicon is a promising anode material for Li-ion batteries due to its high theoretical specific capacity. From previous work, silicon nanowires (SiNWs) are known to undergo amorphorization during lithiation, and no crystalline Li—Si product has been observed. In this work, we use an X-ray transparent battery cell to perform *in situ* synchrotron X-ray diffraction on SiNWs in real time during electrochemical cycling. At deep lithiation voltages the known metastable $Li_{15}Si_4$ phase forms, and we show that avoiding the formation of this phase, by modifying the SiNW growth temperature, improves the cycling performance of SiNW anodes. Our results provide insight on the (de)lithiation mechanism and a correlation between phase evolution and electrochemical performance for SiNW anodes.

KEYWORDS: Li-ion batteries · silicon nanowires · *in situ* X-ray diffraction · (de)lithiation mechanism · phase evolution · electrochemical performance

One of the most sought after renewable energy storage technologies is based on Li-ion batteries (LIBs),[1−4] but so far the existing LIB materials do not meet the growing need for high energy density storage, a result of their limited storage capacity.[5] Silicon is a promising candidate for an anode material in LIBs. Its theoretical capacity, 4200 mA h g^{-1},[6] is the largest among available LIB anode materials and is more than 10 times that of existing commercial graphite (372 mA h g^{-1}).[7] In addition, Si has a low discharge potential *vs* Li/Li^+ and is earth-abundant. However, the large capacity of Si is accompanied by large volume expansion (*ca.* 400%) due to Li-ion insertion, which can induce extensive stress that causes cracking and pulverization of Si anodes.[6] This results in loss of mechanical/electrical contact and capacity fading.[7−12] In an effort to address this problem, silicon nanowire (SiNW) assemblies[13] as Li-ion anodes were developed along with other nanostructured materials.[13−23] Due to their nanoscale diameter, SiNWs allow facile volume expansion while minimizing pulverization and maintaining good electrical contact along the length of the NWs. However, while the (de)lithiation mechanisms in SiNWs have been previously studied,[13] they remain poorly understood due to the lack of *in situ* experiments. To shed light on these mechanisms, we conducted *in situ* X-ray diffraction during SiNW (de)lithiation. At low potentials, we observe the presence of a known metastable $Li_{15}Si_4$ phase. We show that the presence of this crystalline phase degrades the SiNW cycling performance, highlighting the importance of minimizing the repeated amorphous−crystalline transformations upon multiple lithiation−delithiation cycles.

Despite numerous reports on Si anodes, most research activities have focused on micrometer-sized particles and thin films.[9,24−26] Moreover, previous studies on SiNWs have largely been limited to *ex situ* X-ray diffraction (XRD) and transmission electron microscopy (TEM) measurements.[13,27,28] These *ex situ* results showed that upon lithiation crystalline SiNWs transform to a two-phase mixture composed of lithiated amorphous and unlithiated crystalline Si, and by the end of first lithiation cycle lithiated amorphous Si is the only phase present. However, unlike

* Address correspondence to mftoney@slac.stanford.edu; yicui@stanford.edu.

Received for review March 26, 2012 and accepted May 4, 2012.

Published online 10.1021/nn301339g

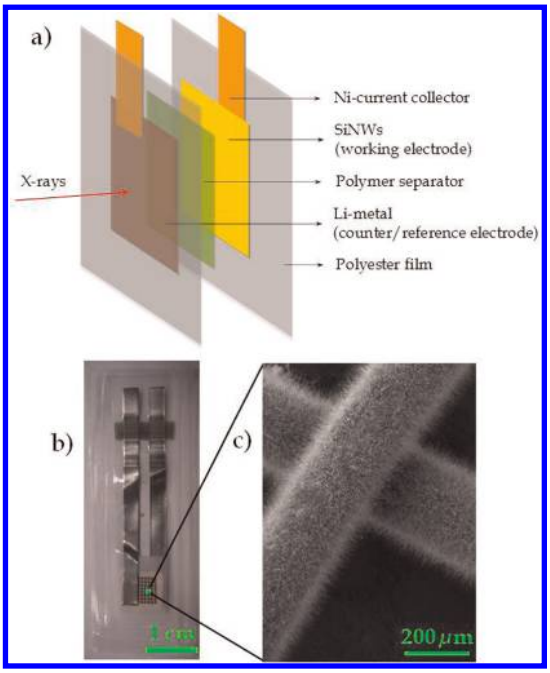

Figure 1. Schematic figure of an *in situ* cell (a) and a picture (b) of the same. The working electrode used is SiNW grown on stainless steel mesh (SS-mesh) by CVD. SEM micrograph (c) shows SiNW on SS-mesh.

for micrometer-sized thin films and particles, no crystalline Li–Si phases were observed. As some of the Li–Si phases are known to be metastable,[25] it is possible that these phases will not be observed with *ex situ* characterization techniques. This motivated us to study these SiNW anodes by means of *in situ* synchrotron X-ray diffraction in real time to study the (de)lithiation mechanisms in SiNWs.

To study these processes, we developed sealed "pouch-type" cells (Figure 1) with X-ray transparent polyester films that allow us to monitor the phase changes *in situ* during electrochemical cycling. The binary Li–Si phase diagram consists of four reported crystalline lithium silicides: $Li_{12}Si_7$, Li_7Si_3, $Li_{13}Si_4$, and $Li_{21}Si_5$.[29–35] However, upon room-temperature electrochemical lithiation, we find that SiNWs do not form any of these phases. From our present results, we observe that as the SiNW cells are electrochemically lithiated, the Si diffraction intensities diminish and new diffraction peaks appear corresponding to three different crystal phases. Two sets of peaks (which we label phase I and II) cannot be indexed to any previously reported Li–Si or Li–electrolyte products and are likely reaction products of Li with the Au catalyst used for SiNW growth. The third sets of peaks was observed only at deep lithiation voltages and was indexed to $Li_{15}Si_4$. In this report, we discuss the origin of these three crystalline phases, their behavior during electrochemical cycles and synthetic growth conditions, and their effect on battery cell performance.

RESULTS AND DISCUSSION

Phase Evolution during Electrochemical Cycling. Previous *ex situ* XRD and TEM results[13] have shown that SiNWs gradually lost their crystallinity upon lithiation and were completely amorphous by the end of the first lithiation cycle. No additional crystalline phases were observed. Our present *in situ* work explains in further detail the reaction mechanism of Li with SiNWs. For these *in situ* experiments, we used two types of SiNW cells. The cells differed in the substrate on which SiNWs were grown. For the first cell (SS-mesh cell) we used stainless steel mesh (SS-mesh) as the substrate. For the second cell (titanium nitride (TiN) cell) we used fused silica substrates coated with TiN to act as the conducting layer between the NWs and the current collector. All other components in both cells were identical. The diffracted intensities were lower for the SS-mesh cells due to higher X-ray absorption by SS-mesh compared to fused silica. On the other hand, the electrical resistance of the TiN layer was high, creating a higher overpotential for the TiN cells compared to the SS-mesh cells, thus limiting TiN cells to just one electrochemical cycle. Since the contact between the current collector and SS-mesh was better, these cells could be cycled multiple times. Below, we present results from SS-mesh cells, and the results from TiN cells are included in the Supporting Information. The phase evolution during the electrochemical cycling of the SiNWs for both these cells was consistent and reproducible. All cells were galvanostatically cycled at a rate of C/5 unless otherwise noted.

Figures 2 and 3 show the *in situ* XRD results for a SS-mesh cell during the first and second galvanostatic lithiation–delithiation cycle, respectively, as a function of amount (x) of Li in Li_xSi, which was calculated according to the specific capacity. Figure 2a shows the XRD pattern at the start of the lithiation cycle. The labeled diffraction peaks are associated with Si (Q = 2.00 (111), 3.27 (220), and 3.84 (311) $Å^{-1}$; JCPDS # 00-005-0565), Li (Q = 2.53 (110) and 3.59 (200) $Å^{-1}$; JCPDS # 01-001-1131), Au (Q = 2.66 (111) and 4.36 (220) $Å^{-1}$; JCPDS # 00-004-0784; catalyst for SiNW growth), and stainless steel (Q = 3.03 (111) and 3.50 (200) $Å^{-1}$; JCPDS # 00-003-0397). All unlabeled peaks are associated with either the polyester pouch or polymer separator (Q = 1.52, 1.69, 2.78, 2.84, and 2.90 $Å^{-1}$ and other low-intensity peaks). Figure 2b and c contain expanded Q-space sections of Figure 2a, indicated by rectangular boxes, as the SiNWs undergo lithiation–delithiation as per the voltage profile shown in Figure 2d. Figure 3a and b show *in situ* XRD results on the same SS-mesh cell for the second lithiation–delithiation cycle as per the voltage profile shown in Figure 3d.

As the SiNWs are lithiated, the Si(111) diffraction intensity diminishes (Figure 2c). This is consistent with previous reports of disappearance of crystalline Si and

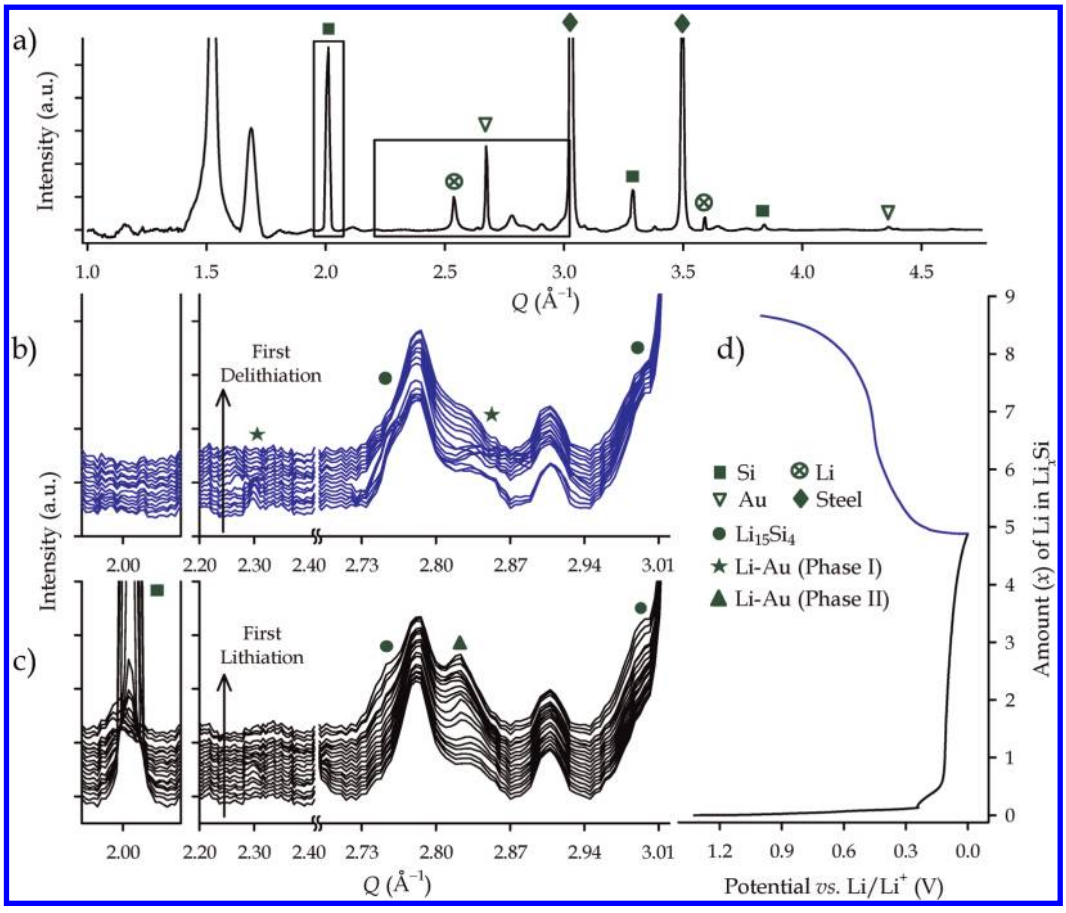

Figure 2. *In situ* **XRD results for a SS-mesh cell cycled at C/5: (a) XRD pattern at the start of the lithiation cycle, (b and c) XRD patterns showing zoomed-in sections of *Q*-space regions shown in (a) for the first lithiation and delithiation cycle, respectively, and (d) voltage profile showing the first cycle as a function of the amount (*x*) of Li in Li_xSi. Unlabeled peaks are associated with either the polyester pouch or polymer separator.**

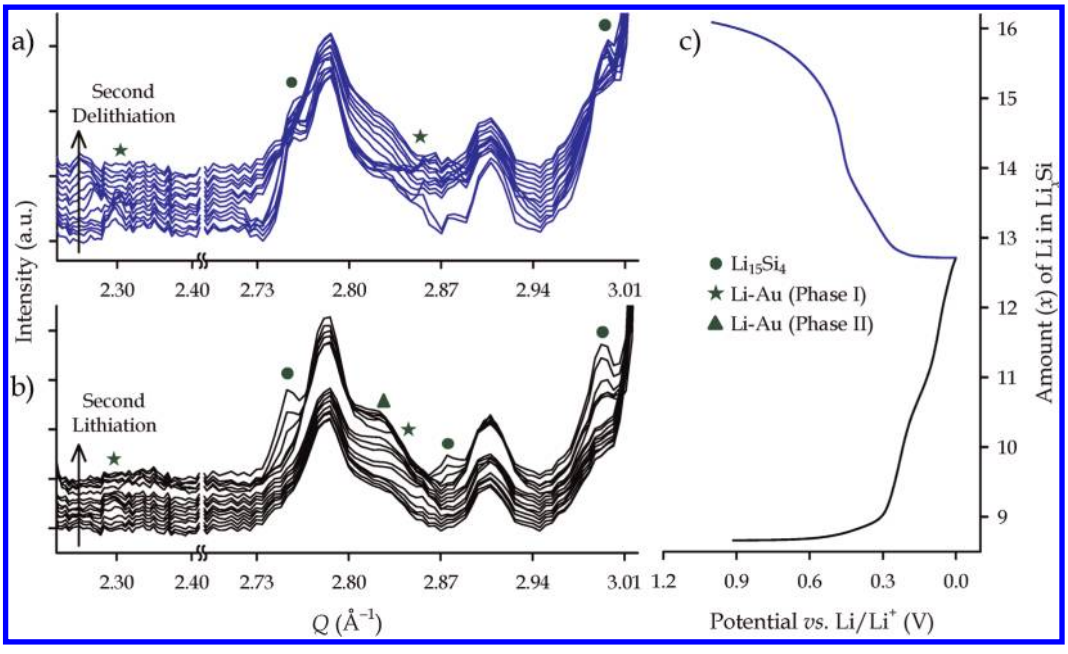

Figure 3. *In situ* **XRD results for the same SS-mesh cell shown in Figure 2 cycled at C/5: (a and b) XRD patterns for the second lithiation and delithiation cycle, respectively, and (c) voltage profile showing the second cycle as a function of the amount (*x*) of Li in Li_xSi. Unlabeled peaks are associated with either the polyester pouch or polymer separator.**

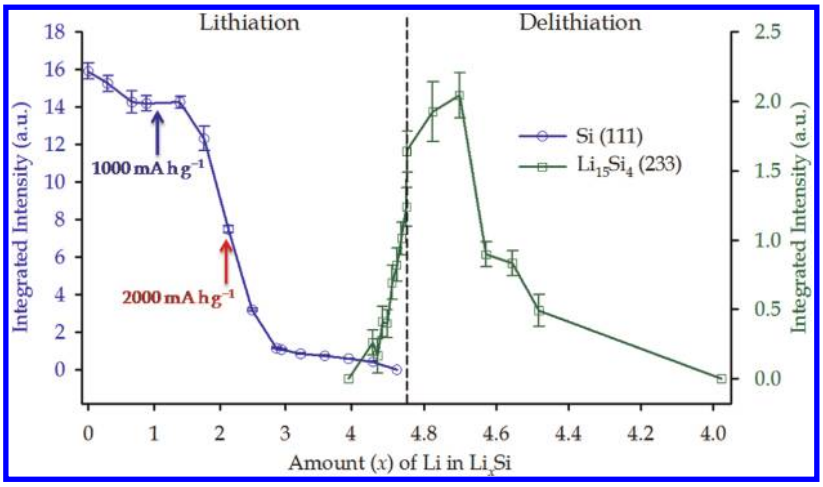

Figure 4. Integrated intensities for Si(111) and $Li_{15}Si_4$(233) peaks for the same SS-mesh cell shown in Figure 2, cycled at C/5, plotted as function of amount (*x*) of Li in Li_xSi. The arrows show the corresponding values of specific capacity (1000 and 2000 mA h g^{-1}), which guided the constant capacity cycling experiments.

formation of amorphous Li_xSi, which also results in a voltage plateau (Figure 2d) that is indicative of two-phase coexistence (crystalline Si and amorphous Li−Si). A plot of the integrated intensity as a function of *x* for the Si(111) peak (Figure 4) during the first lithiation cycle shows the decrease in peak intensity. Upon further lithiation, five new diffraction peaks (Figures 2, 3, S1, and S2) at Q = 1.66, 1.69, 2.29, 2.83, and 2.93 Å^{-1} appear, which we label as phase I. These phase I peaks were not observed for cells with other morphologies of Si and could not be indexed to known products resulting from reaction between the electrolyte with Li nor to any of the known Si−Au and Li−Si phases. As the lithiation of SiNWs progresses further, three other new diffraction peaks (Figures 2, 3, S1, and S2) at Q = 1.72, 2.81, and 3.29 Å^{-1} appear, which we label as phase II, while the phase I peaks decrease. When changing the current direction to delithiate the SiNWs, the phase II peaks immediately disappeared and the phase I peaks reappeared (Figures 2 and 3). Figure S3 shows how the integrated intensities for the diffraction peaks corresponding to phase I and II change with (de)lithiation for a TiN cell. To determine whether these new phases are Li−Si phases, we performed control experiments with Au film and Au nanoparticles without any Si. These results, which are discussed below, indicate the phases are due to reaction of Li with Au.

At very low potentials *vs* Li/Li$^+$ (<20 mV), we observed diffraction peaks corresponding to $Li_{15}Si_4$ at Q = 2.76 (233), 2.88 (224), and 2.99 (015) Å^{-1} (Figures 2 and 3) and Q = 1.44 (112), 1.66 (022), 1.86 (013) Å^{-1} (not shown). Figure 4 shows a plot of the integrated intensity as a function of *x* for the $Li_{15}Si_4$ (233) peak. The intensity reaches a maximum in the delithiation cycle for x = 4.70. Upon further delithiation, its diffraction intensity diminishes and crystalline $Li_{15}Si_4$ disappears completely by x = 3.98. No crystalline Si peaks form in the delithiation cycle. This suggests that crystalline $Li_{15}Si_4$ is delithiated to form amorphous Li_xSi, constituting a two-phase region (crystalline $Li_{15}Si_4$ and amorphous Li_xSi). This observation of $Li_{15}Si_4$ is in contrast to previous *ex situ* studies[13] on SiNWs, but similar to *in situ* studies on other Si electrode morphologies.[9,24−26] The absence of $Li_{15}Si_4$ phase in *ex situ* studies shows the transient nature of this phase, which is not surprising, as it is also absent in a binary Li−Si phase diagram. These results highlight the importance of *in situ* studies on energy storage materials.[36]

By cycling the SiNWs up to three times in the SS-mesh cells and tracking the phase evolution with *in situ* X-ray diffraction, we observed that the evolution of phase I and II and $Li_{15}Si_4$ is reversible in subsequent electrochemical cycles. Interestingly, the diffraction intensities for all these phases are higher in the second electrochemical cycle compared to the first. This feature is not well understood.

To gain further insight into the electrochemical stability of these crystalline phases, we studied these SiNW cells under electrochemical relaxation conditions. These results, details of which are included in the Supporting Information, show that if the SiNW cells are relaxed and material homogenization is allowed at potentials of ~45 mV, the formation of crystalline $Li_{15}Si_4$ at lower potentials can be inhibited. Moreover, if the relaxation experiment is performed after $Li_{15}Si_4$ appears, then the $Li_{15}Si_4$ diffraction peak intensities (Figure S6) increase during the initial relaxation process. Also, as shown in Figure 4, the $Li_{15}Si_4$ intensities continue to increase after the current is reversed. Both these results indicate that the formation of $Li_{15}Si_4$ is kinetically limited. On this basis, we speculate that faster cycling of SiNWs can limit the amount of formation of crystalline $Li_{15}Si_4$.

Electrochemical Lithiation Experiments with Au. Two control experiments were designed to understand if phase I and II were due to the electrochemical reaction of Au

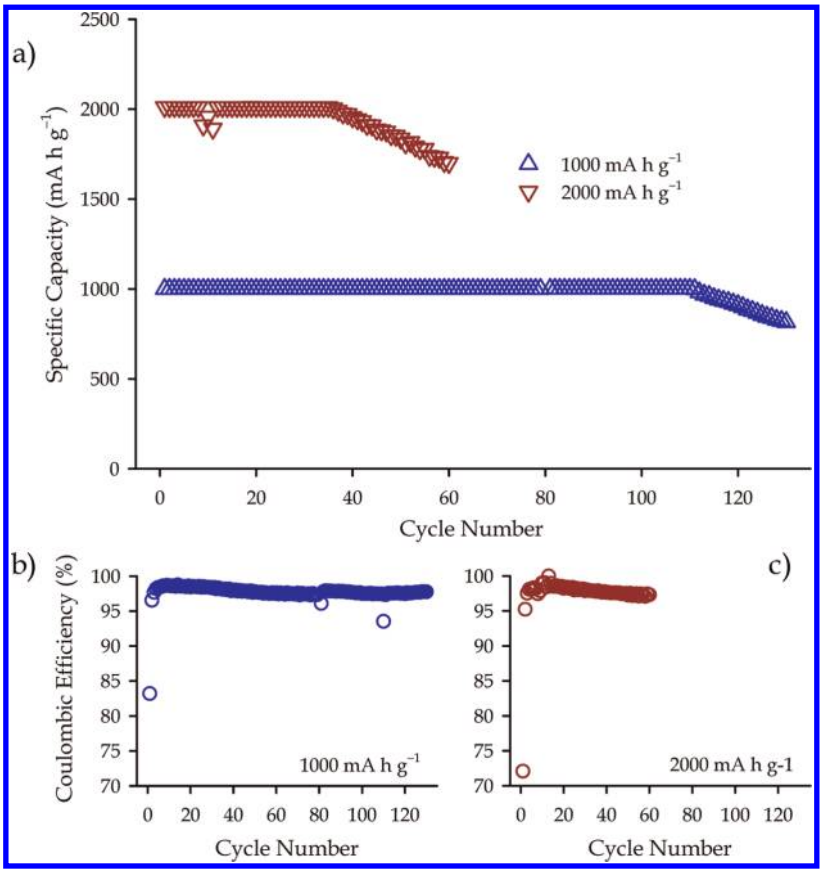

Figure 5. Constant capacity cycling performance of SiNW anodes: (a) cycled at constant capacity of 1000 mA h g^{-1} (blue) and 2000 mA h g^{-1} (dark red); only lithiation capacities are shown; (b and c) Coulombic efficiencies for the two cells.

with Li. For the first experiment, a 50 nm thick Au film on SS-mesh was used as the electrode, and for the second experiment, Au nanoparticles on a SS-mesh electrode was used. For the first cell, no peaks matching phase I and II were observed, but for the second cell (Figure S4), peaks corresponding to both phase I (Q = 1.66, 1.69, 2.29, 2.83, and 2.93 Å^{-1}) and phase II (Q = 1.72, 2.81, and 3.29 Å^{-1}) were observed. This difference in phase evolution between Au film and nanoparticle is possibly due to the difference in stress during lithiation of different Au morphologies. The Au nanoparticle results show that the crystal structures of phase I and II are similar to Li–Au alloys, although it is possible that these are ternary Li–Au–Si phases. However, since no such Li–Si binary phases were observed for other Si morphologies,[24–26] we conclude that phase I and II are Li–Au phases. Some of the phase I and II diffraction peak positions are similar to the new Li–Au phases reported by Taillades *et al.*[37] and Renner *et al.*,[38] but due to the limited number of observed Bragg peaks for these new phases, complete peak indexing was not possible. Hence, the crystal structures of these Li–Au phases remain unknown.

In order to understand the relationship between these observed crystalline phases, especially $Li_{15}Si_4$, and the electrochemical reaction of Li with the SiNWs, we studied this anode material under various conditions as discussed below.

Constant Capacity Cycling. The Si(111) integrated intensity as a function of the extent of lithiation (Figure 4) does not show any significant change up to x = 1.39 (specific capacity = 1330 mA h g^{-1}), which is similar to previous reports.[24] This figure highlights that the initial crystallinity of SiNWs does not change significantly even when the initial Li_xSi alloy is formed, as also observed from the voltage plateau (Figure 2). It is noteworthy that the maximum lithiation extent (either in x or specific capacity) where the Si(111) integrated intensity does not change significantly is greater for SiNWs (x = 1.39) compared to Si micrometer sized particles (x = 0.52).[24,39] To understand how this impacts the cycling performance of SiNWs, we designed two constant capacity cycling experiments.[40] The first cell was cycled at a lower constant capacity of 1000 mA h g^{-1} (x = 1.05), and the second cell was limited to a higher constant capacity of 2000 mA h g^{-1} (x = 2.10). Figure 5 shows the cycling performance of these two cells and their Coulombic efficiencies. The first cell performs excellently for 110 cycles before showing capacity fading, whereas the second cell starts showing capacity fading after only 36 cycles, although their Coulombic efficiencies are very similar (~98%).

In alloy anodes for LIBs, crystalline–amorphous–crystalline transformations upon lithiation are seen as detrimental.[41,42] Thus, our results show that a possible

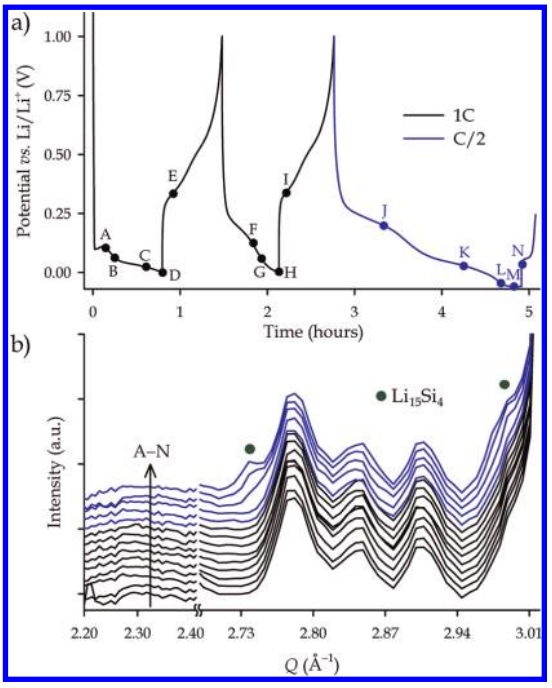

Figure 6. *In situ* **XRD results for a SS-mesh cell under electrochemical cycling: (a) voltage profile for a cell cycled at 1C (black) and C/2 (blue); (b) XRD patterns showing the appearance of $Li_{15}Si_4$ peaks for corresponding points A−N in (a). Unlabeled peaks are associated with either the polyester pouch or polymer separator.**

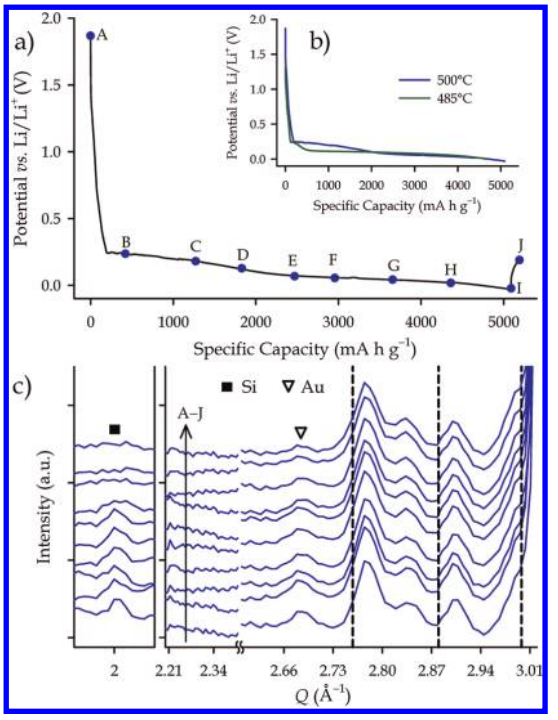

Figure 7. *In situ* **XRD results for a SS-mesh cell containing SiNWs grown by CVD at 500 °C under electrochemical cycling: (a) voltage profile for a cell cycled at C/5; (b) comparison of the first lithiation cycle voltage profiles for SiNWs grown at 500 °C (blue) and 485 °C (dark green). The blue plot shows two plateaus during first lithiation, which is a signature of poorly crystalline Si, and the dark green plot shows a single plateau expected of crystalline Si. (c) XRD patterns showing the absence of diffraction peaks corresponding to any crystalline Li−Si and Li−Au phases for A−J corresponding points in (a). The Si peak intensities are weak, showing the poor crystallinity of SiNWs grown at 500 °C. The vertical dashed lines show where $Li_{15}Si_4$ peaks should be observed. Unlabeled peaks are associated with either the polyester pouch or polymer separator.**

strategy to improve cycle stability in crystalline SiNW anodes is to only cycle to a lower specific capacity cutoff. Since cycling to a lower capacity does not significantly change the crystallinity of the lithiated SiNWs (Figure 4), we speculate that this mitigates the stress buildup due to Li^+ insertion/extraction and, thereby, results in capacity retention for a greater number of electrochemical cycles in comparison to cycling to a higher capacity. Although, our strategy of cycling SiNWs at ~1000 mA h g^{-1} does not utilize the full capacity of Si, the capacity is still more than 2.5 times greater than existing commercial graphite anodes.

Cycling Rate. To probe the dependence of the phase evolution behavior on the cycling rate, multiple cells were cycled at C/20, C/10, C/5, C/2, and 1C. For slower cycling rates (C/20, C/10, and C/5), the phase evolution occurred as discussed above (formation of phase I and II and $Li_{15}Si_4$). However, when a SiNW anode was cycled at a faster charge rate (1C and C/2), no crystalline phases were observed for potentials as low as zero volts (Figure 6). Only when the cell was driven to −42 mV *vs* Li/Li^+ at C/2 did we observe diffraction peaks from $Li_{15}Si_4$. Intriguingly, phase I and II (Li−Au phases) did not crystallize at 1C and C/2 cycling rates. These results suggest that stress generated in the SiNWs by faster Li^+ insertion/extraction affects the phase evolution behavior of not only Li−Si but also Li−Au alloy systems.

SiNW Chemical Vapor Deposition (CVD) Growth Temperature. To understand the relationship between the observed phase evolution and synthetic SiNW growth conditions, we studied SiNW anodes grown at various CVD temperatures. For the cells with SiNWs on SS-mesh, we employed three different growth temperatures: 470, 485, and 500 °C. Changes were observed in the crystallinity, electrochemical behavior, and the *in situ* phase evolution as the temperature was increased. Comparing the Si(111) integrated peak intensities, we conclude that the crystallinity of SiNWs decreased with increasing CVD growth temperature, which is consistent with previous reports.[43,44]

Figure 7 shows the *in situ* XRD results for a 500 °C sample. These SiNWs were poorly crystalline, as they showed weak Si peaks (Figure 7c). This is also evident from the electrochemistry, which exhibits two plateau regions (Figure 7b blue line) in the first lithiation cycle[9] compared to a single plateau present for crystalline Si samples grown at 485 °C (Figure 7b dark green line). For samples grown at 470 and 485 °C, the *in situ* phase evolution proceeded as explained above. Surprisingly, for the samples grown at 500 °C, none of the crystalline Li−Si or Li−Au phases were observed for voltages down to −30 mV (Figure 7c). This is in contrast with

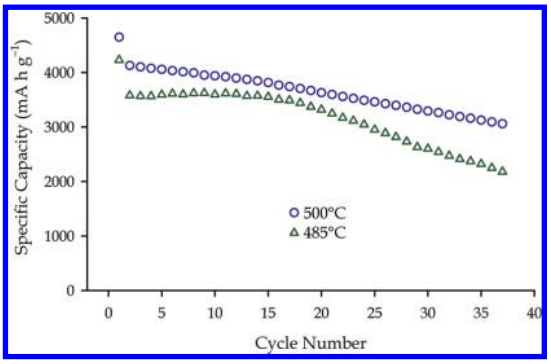

Figure 8. Cycling performance of SiNW samples grown by CVD at 500 and 485 °C. Only lithiation capacities are shown. The SiNWs grown at 500 °C show 33% better capacity retention after 37 cycles compared to SiNWs grown at 485 °C.

other studies performed on 2 μm thick *a*-Si films, which showed the presence of at least $Li_{15}Si_4$.[9] However, these results are similar to studies[9] performed on 0.5 μm thick *a*-Si films, which showed the absence of the crystalline $Li_{15}Si_4$ phase, even when cycled 10 times. The absence of any crystalline alloy phases in the 500 °C grown samples might be due to differences in stress in the SiNWs or to the presence of a different NW near-surface structure of the SiNWs.

Finally, we compared the cycling performance of samples grown at 485 and 500 °C. The cells with SiNWs grown at 500 °C showed 33% better capacity retention after 37 cycles (Figure 8) compared to cells with SiNWs grown at 485 °C. We believe that the absence of crystalline phases during cycling of SiNWs grown at 500 °C is responsible for its improved cycling performance. This again shows that avoiding repeated amorphous−crystalline (*a*-Si to *c*-$Li_{15}Si_4$) transformation upon multiple lithiation−delithiation cycles is a critical factor for better capacity retention. However, additional factors, such as a variation in the SEI layer, may also affect the capacity fade mechanism for these two growth conditions. Furthermore, these conclusions also portray a synthetic controlling tool, such as CVD growth temperature, to modify the phase evolution during (de)lithiation of SiNWs, thereby improving the cycling performance.

CONCLUSION

We have conducted *in situ* X-ray diffraction on SiNW anodes under various cycling rates and with different crystallinity to gain a better understanding of the (de)lithiation mechanism. We propose a strategy to enhance the cycling performance of SiNW anodes by limiting the cycles to a lower specific capacity cutoff. At low potentials, we find the presence of a known metastable $Li_{15}Si_4$ phase. Our results show that the presence of this crystalline phase degrades cycling performance compared to SiNWs, where no intermediate crystalline phases are formed, and the formation of this crystalline phase is correlated with the SiNW growth temperature. Furthermore, we identified two new crystalline Li−Au phases, labeled as phase I and II, and showed that their formation is dependent on the cycling rates and growth temperatures of SiNWs.

EXPERIMENTAL SECTION

Synthesis of Si Nanowires. SiNWs were synthesized using the vapor−liquid−solid growth method via chemical vapor deposition on either stainless steel mesh (stainless steel 304, 100 mesh, TWP Inc.) or 150 μm thick fused silica substrates (FSS) coated with 50 nm thick TiN deposited in an AJA sputtering system.[45] Both substrates were decorated with a 50 nm Au catalyst film obtained by thermal evaporation. The substrates were heated to 470, 485, or 500 °C, and a flow of silane (2% SiH_4 diluted in Ar) was established at 80 sccm for 30 min with a total chamber pressure of 30 Torr. The mass of the SiNWs in a given experiment (*ca.* 250 μg) was determined by measuring the mass of the substrate using a microbalance (Sartorius SE2, 0.1 μg resolution) before and after growth.

***In Situ* XRD Cell and Electrochemistry.** The *in situ* battery cells were fabricated from a SiNW/SS-mesh (Figure 1) or SiNW/FSS electrode, Li metal as the counter electrode, and a Celgard separator soaked in electrolyte. The electrolyte was 1.0 M $LiPF_6$ in 1:1 (w/w) ethylene carbonate/diethyl carbonate (EMD Chemicals). No binders or conducting carbon was used. The cells were assembled inside an Ar-filled glovebox and sealed in 0.11 mm thick transparent polyester pouches (Kapak Corporation). For efficient sealing of the battery cells, pretaped Ni current collectors (MTI Corporation) were used. *In situ* battery cycling was performed using a MTI eight-channel battery analyzer (0.002−1 mA). The voltage cutoffs were typically 1.0 and 0 V *vs* Li/Li^+, and the cycling rate was typically C/5 in terms of the theoretical capacity of SiNWs (4200 mA h g^{-1}). A cycling rate of C/5 means charge/discharge in 5 h.

***In Situ* XRD Cell with Au Film and Au Nanoparticles.** For the Au film cell, SS-mesh (stainless steel 304, 100 mesh, TWP Inc.) was coated with 50 nm Au by thermal evaporation. For the Au nanoparticle cell, Au nanopowder (0.5−0.8 μm, 99.96+%, Alfa Aesar) was made into an aqueous slurry with carbon black (Super P, TIMCAL, Switzerland) and sodium carboxymethylcellulose (CMC) binder (mol wt = 90 000, Aldrich). The weight percent ratio for the electrode was 45% Au, 45% carbon, 10% binder. SS-mesh (stainless steel 304, 400 mesh, TWP Inc.) was dip-coated with this slurry and baked in a vacuum oven at 90 °C for >3 h before cell assembly. The calculated capacity is based only on the weight of Au. All other experimental details were the same as the SiNW cells.

Synchrotron X-ray Diffraction. XRD measurements were performed at the Stanford Synchrotron Radiation Lightsource (SSRL) using beamline 11-3 with a photon wavelength of 0.9744(2) Å. Measurements were done in transmission mode on pouch cells. The detector was located at a distance of 300, 180, or 145 mm from the sample center. The beam size on the sample was 50 μm × 50 μm. The scattering intensity was detected on a 2D image plate (MAR-345) with a pixel size of 150 μm (2300 × 2300 pixels). Exposure time varied from 80 to 210 s, and data were collected in 5 min intervals. The data were distortion corrected (θ-dependent image distortion introduced by planar detector surface) before performing quantitative analysis. Data were internally calibrated using the stainless steel diffraction peaks and analyzed using the Area Diffraction Machine (ADM) software package.[46] WinPlotr,[47] which is part of FullProf Suite Program (1.10),[48] was used for background subtraction.

Conflict of Interest: The authors declare no competing financial interest.

Acknowledgment. We thank F. U. Renner for his valuable comments. Portions of this research were carried out at the

Stanford Synchrotron Radiation Lightsource, a national user facility operated by Stanford University on behalf of the U.S. Department of Energy, Office of Basic Energy Sciences. This work is supported by the Department of Energy, Laboratory Directed Research and Development funding, under contract DE-AC02-76SF00515 (J.N., M.F.T., Y.C.). Y.C. acknowledges support from the King Abdullah University of Science and Technology (KAUST) Investigator Award (No. KUS-I1-001-12).

Supporting Information Available: Additional *in situ* XRD and electrochemical experimental details and results. This material is available free of charge via the Internet at http://pubs.acs.org.

REFERENCES AND NOTES

1. Whittingham, M. S. Lithium Batteries and Cathode Materials. *Chem. Rev.* **2004**, *104*, 4271–4301.
2. Armand, M.; Tarascon, J. M. Building Better Batteries. *Nature* **2008**, *451*, 652–657.
3. Armand, M.; Tarascon, J. M. Issues and Challenges Facing Rechargeable Lithium Batteries. *Nature* **2001**, *414*, 359–367.
4. Goodenough, J. B.; Kim, Y. Challenges for Rechargeable Li Batteries. *Chem. Mater.* **2010**, *22*, 587–603.
5. Annual Progress Report on Energy Storage Research and Development, U.S. Department of Energy, 2010.
6. Boukamp, B. A.; Lesh, G. C.; Huggins, R. A. All-Solid Lithium Electrodes with Mixed-Conductor Matrix. *J. Electrochem. Soc.* **1981**, *128*, 725–729.
7. Beaulieu, L. Y.; Eberman, K. W.; Turner, R. L.; Krause, L. J.; Dahn, J. R. Colossal Reversible Volume Changes in Lithium Alloys. *Electrochem. Solid State Lett.* **2001**, *4*, A137–A140.
8. Besenhard, J. O.; Yang, J.; Winter, M. Will Advanced Lithium-Alloy Anodes Have a Chance in Lithium-ion Batteries?. *J. Power Sources* **1997**, *68*, 87–90.
9. Hatchard, T. D.; Dahn, J. R. *In Situ* XRD and Electrochemical Study of the Reaction of Lithium with Amorphous Silicon. *J. Electrochem. Soc.* **2004**, *151*, A838–A842.
10. Raimann, P. R.; Hochgatterer, N. S.; Korepp, C.; Möller, K. C.; Winter, M.; Schröttner, H.; Hofer, F.; Besenhard, J. O. Monitoring Dynamics of Electrode Reactions in Li-Ion Batteries by *In Situ* ESEM. *Ionics* **2006**, *12*, 253–255.
11. Weydanz, W. J.; Wohlfahrt-Mehrens, M.; Huggins, R. A. A Room Temperature Study of the Binary Lithium-Silicon and the Ternary Lithium-Chromium-Silicon System for Use in Rechargeable Lithium Batteries. *J. Power Sources* **1999**, *81*, 237–242.
12. Zhang, X. W.; Patil, P. K.; Wang, C.; Appelby, A. J.; Little, F. E.; Cocke, D. L. Electrochemical Performance of Lithium Ion Battery, Nano-Silicon-Based, Disordered Carbon Composite Anodes with Different Microstructures. *J. Power Sources* **2004**, *125*, 206–213.
13. Chan, C. K.; Peng, H.; Liu, G.; McIlwrath, K.; Zhang, X. F.; Huggins, R. A.; Cui, Y. High-Performance Lithium Battery Anodes Using Silicon Nanowires. *Nat. Nanotechnol.* **2008**, *3*, 31–35.
14. Cui, L. F.; Ruffo, R.; Chan, C. K.; Peng, H. L.; Cui, Y. Crystalline-Amorphous Core-Shell Silicon Nanowires for High Capacity and High Current Battery Electrodes. *Nano Lett.* **2009**, *9*, 491–495.
15. Cui, L. F.; Yang, Y.; Hsu, C. M.; Cui, Y. Carbon-Silicon Core-Shell Nanowires as High Capacity Electrode for Lithium Ion Batteries. *Nano Lett.* **2009**, *9*, 3370–3374.
16. Hertzberg, B.; Alexeev, A.; Yushin, G. Deformations in Si-Li Anodes upon Electrochemical Alloying in Nano-Confined Space. *J. Am. Chem. Soc.* **2010**, *132*, 8548–8549.
17. Kim, H.; Han, B.; Choo, J.; Cho, J. Three-Dimensional Porous Silicon Particles for Use in High-Performance Lithium Secondary Batteries. *Angew. Chem., Int. Ed.* **2008**, *47*, 10151–10154.
18. Kim, H.; Seo, M.; Park, M. H.; Cho, J. A Critical Size of Silicon Nano-Anodes for Lithium Rechargeable Batteries. *Angew. Chem., Int. Ed.* **2010**, *49*, 2146–2149.
19. Magasinski, A.; Dixon, P.; Hertzberg, B.; Kivit, A.; Ayala, J.; Yushin, G. High-Performance Lithium-Ion Anodes Using a Heirarchical Bottom-Up Approach. *Nat. Mater.* **2010**, *9*, 353–358.
20. Park, M. H.; Kim, M. G.; Joo, J.; Kim, K.; Kim, J.; Ahn, S.; Cui, Y.; Cho, J. Silicon Nanotube Battery Anodes. *Nano Lett.* **2009**, *9*, 3844–3847.
21. Peng, K.; Jie, J.; Zhang, W.; Lee, S. T. Silicon Nanowires for Rechargeable Lithium-Ion Battery Anodes. *Appl. Phys. Lett.* **2008**, *93*, 033105/1–033105/3.
22. Song, T.; Xia, J.; Lee, J. H.; Lee, D. H.; Kwon, M. S.; Choi, J. M.; Wu, J.; Doo, S. K.; Chang, H.; Park, W. I.; *et al*. Arrays of Sealed Silicon Nanotubes as Anodes for Lithium Ion Batteries. *Nano Lett.* **2010**, *10*, 1710–1716.
23. Yao, Y.; McDowell, M. T.; Ryu, I.; Wu, H.; Liu, N.; Hu, L.; Nix, W. D.; Cui, Y. Interconnected Silicon Hollow Nanospheres for Lithium-Ion Battery Anodes with Long Cycle Life. *Nano Lett.* **2011**, *11*, 2949–2954.
24. Li, J.; Dahn, J. R. An *In Situ* X-Ray Diffraction Study of the Reaction of Li with Crystalline Si. *J. Electrochem. Soc.* **2007**, *154*, A156–A161.
25. Key, B.; Bhattacharyya, R.; Morcrette, M.; Seznéc, V.; Tarascon, J. M.; Grey, C. P. Real Time NMR Investigations of Structural Changes in Silicon Electrodes for Lithium-Ion Batteries. *J. Am. Chem. Soc.* **2009**, *131*, 9239–9249.
26. Key, B.; Morcrette, M.; Tarascon, J. M.; Grey, C. P. Pair Distribution Function Analysis and Solid State NMR Studies of Silicon Electrodes for Lithium Ion Batteries: Understanding the (De)lithiation Mechanisms. *J. Am. Chem. Soc.* **2010**, *133*, 503–512.
27. Recently, *in situ* TEM studies[28] were performed on SiNWs cells using ionic liquids as electrolyte (instead of the typical commercial electrolyte) where the anodes were only partly immersed. While these provided insight into the lithiation process, some artifacts may have been created by this setup. Hence, these results are not included in our discussion in this report.
28. Liu, H. C.; Zhang, L. Q.; Zhong, L.; Liu, Y.; Zheng, H.; Wang, J. W.; Cho, J. H.; Dayeh, S. A.; Picraux, A. T.; Sullivan, J. P.; *et al*. Ultrafast Electrochemical Lithiation of Individual Si Nanowire Anodes. *Nano Lett.* **2011**, *11*, 2251–2258.
29. Nesper, R. Structure and Chemical Bonding in Zintl-Phases Containing Lithium. *Prog. Solid State Chem.* **1990**, *20*, 1–45.
30. Schnering, H. G. v.; Nesper, R.; Curda, J.; Tebbe, K. –F. $Li_{12}Si_7$, a Compound Having a Trigonal Planar Si_4 Cluster and Planar Si_5 Rings. *Angew. Chem., Int. Ed. Engl.* **1980**, *19*, 1033–1034.
31. Nesper, R.; Schnering, H. G. v.; Curda, J. $Li_{12}Si_7$, To Connect with Trigonal-Planar Si_4-Cluster and Isometric Si_5-Rings. *Chem. Ber.* **1986**, *119*, 3576–3590.
32. Klemm, W.; Struck, M. Notiz über die Verbindungen zwischen Lithium und Silicium. *Z. Anorg. Allg. Chem.* **1955**, *278*, 117–121.
33. Schnering, H. G. v.; Nesper, R.; Tebbe, K. –F.; Curda, J. Structure and Properties of $Li_{14}Si_6$ ($Li_{2.33}Si$) the Purple Phase in the System Lithium–Silicon. *Z. Metallkd.* **1980**, *71*, 357–363.
34. Frank, U.; Muller, W.; Schafer, H. Phase $Li_{13}Si_4$. *Z. Naturforsch.* **1975**, *B30*, 10–13.
35. Nesper, R.; Schnering, H. G. v. $Li_{21}Si_5$, a Zintl Phase as well as a Hume-Rothery Phase. *J. Solid State Chem.* **1987**, *70*, 48–57.
36. Nelson, J.; Misra, S.; Yang, Y.; Jackson, A.; Liu, Y.; Wang, H.; Dai, H.; Andrews, J. C.; Cui, Y.; Toney, M. F. *In Operando* X-ray Diffraction and Transmission X-ray Microscopy of Lithium Sulfur Batteries. *J. Am. Chem. Soc.* **2012**, *134*, 6337–6343.
37. Taillades, G.; Benjelloun, N.; Sarradin, J.; Ribes, M. Metal-based Very Thin Film Anodes for Lithium Ion Microbatteries. *Solid State Ion.* **2002**, *152–153*, 119–124.
38. Renner, F. U.; Kageyama, H.; Siroma, Z.; Shikano, M.; Schöder, S.; Gründer, Y.; Sakata, O. Gold Model Anodes for Li-ion Batteries: Single Crystalline Systems Studied by *in Situ* X-ray Diffraction. *Electrochem. Acta* **2008**, *53*, 6064–6069.
39. The battery cells used in ref 24 contained micrometer-sized Si particles, super P carbon black, and CMC binder, and the cells were cycled at C/100. The extent in *x* (or specific capacity) up to which the Si(111) integrated

intensity does not show significant change may be affected by the anode morphology, composition, and cycling rate, and hence a direct comparison cannot be made with our SiNW cells.

40. Cui, L.-F.; Hu, L.; Wu, H.; Choi, J. W.; Cui, Y. Inorganic Glue Enabling High Performance of Silicon Particles as Lithium Ion Battery Anode. *J. Electrochem. Soc.* **2011**, *158*, A592–A596.
41. Beaulieu, L. Y.; Hatchard, T. D.; Bonakdarpour, A.; Fleischauer, M. D.; Dahn, J. R. Reaction of Li with Alloy Thin Films Studied by *in Situ* AFM. *J. Electrochem. Soc.* **2003**, *150*, A1457–A1464.
42. Chevrier, V. L.; Zwanziger, J. W.; Dahn, J. R. First Principles Study of Li−Si Crystalline Phases: Charge Transfer, Electronic Structure, and Lattice Vibrations. *J. Alloys Compd.* **2010**, *496*, 25–36.
43. Chen, H.; Xu, J.; Chen, P.; Fang, X.; Qiu, J.; Fu, Y.; Zhou, C. Bulk Synthesis of Crystalline and Crystalline Core/Amorphous Shell Silicon Nanowires and Their Application for Energy Storage. *ACS Nano* **2011**, *5*, 8383–8390.
44. Dong, Y.; Yu, G.; McAlpine, M. C.; Lu, W.; Lieber, C. M. Si/a-Si Core/Shell Nanowires as Nonvolatile Crossbar Switches. *Nano Lett.* **2008**, *8*, 386–391.
45. Meister, S.; Kim, S.; Cha, J. J.; Wong, H. S.; Cui, Y. *In Situ* Transmission Electron Microscopy Observation of Microstructural Changes in Phase-Change Memory. *ACS Nano* **2011**, *5*, 2742–2748.
46. Lande, J.; Webb, S. M.; Mehta, A. *Area Diffraction Machine*, **2008**, http://code.google.com/p/areadiffractionmachine/.
47. Roisnel, T.; Rodriguez-Carvajal, J. WinPLOTR: A Windows Tool for Powder Diffraction Pattern Analysis. *Mater. Sci. Forum* **2001**, *378−381*, 118–123.
48. Rodriguez-Carvajal, J. Recent Advances in Magnetic Structure Determination by Neutron Powder Diffraction. *Phys. B* **1993**, *192*, 55–69.